Journal Pre-proof

Adsorption of As(V) and Ni(II) by Fe-Biochar Composite Fabricated by Co-pyrolysis of Orange Peel and Red Mud

Kwangsuk Yoon, Dong-Wan Cho, Amit Bhatnagar, Hocheol Song

Please cite this article as: Yoon, K., Cho, D.-W., Bhatnagar, A., Song, H., Adsorption of As(V) and Ni(II) by Fe-Biochar Composite Fabricated by Co-pyrolysis of Orange Peel and Red Mud, *Environmental Research*, https://doi.org/10.1016/j.envres.2020.109809.

This is a PDF file of an article that has undergone enhancements after acceptance, such as the addition of a cover page and metadata, and formatting for readability, but it is not yet the definitive version of record. This version will undergo additional copyediting, typesetting and review before it is published in its final form, but we are providing this version to give early visibility of the article. Please note that, during the production process, errors may be discovered which could affect the content, and all legal disclaimers that apply to the journal pertain.

Adsorption of As(V) and Ni(II) by Fe-Biochar Composite Fabricated by Co-pyrolysis of Orange Peel and Red Mud

Kwangsuk Yoon [a,†], Dong-Wan Cho [b,†], Amit Bhatnagar [c], and Hocheol Song [a,*]

[a] *Department of Environment and Energy, Sejong University, Seoul 05006, Republic of Korea*

[b] *Geologic Environment Division, Korea Institute of Geoscience and Mineral Resources (KIGAM), Daejeon 34132, Republic of Korea*

[c] *Department of Environmental and Biological Sciences, University of Eastern Finland, P.O. Box 1627, Fl-70211, Kuopio, Finland*

[†] These authors equally contributed to this work

[*] Corresponding author:
Name: Hocheol Song
Address: 209 Neungdong-Ro, Gwangjin-Gu, Seoul, 05006 South Korea
Tel: 82 2 3408 3232
e-mail: hcsong@sejong.ac.kr

ABSTRACT

This study aimed to compare the adsorption performance of Fe-biochar composites (Fe-C-N_2 and Fe-C-CO_2), fabricated by co-pyrolysis of red mud and orange peel in N_2 and CO_2, for As(V) and Ni(II). By the syngas production comparison test, it was confirmed that CO_2 was more advantageous than N_2 as a pyrolytic medium gas to produce more CO. The resulting Fe-biochar composite showed the aggregate morphology consisting of different Fe phases (magnetite or metal Fe) from the inherent hematite phase in red mud and carbonized carbon matrix, and there was no distinct difference between the structural shapes of two Fe-biochar composites. Adsorption experiments showed that the adsorption capacities for As(V) and Ni(II) in single mode were almost similar with 7.5 and 16.2 mg g^{-1} for Fe-C-N_2 and 5.6 and 15.1 mg g^{-1} for Fe-C-CO_2, respectively. The adsorption ability of Fe-C-CO_2 for both As(V) and Ni(II) was further enhanced in binary adsorption mode (As(V): 13.4 mg g^{-1}, Ni(II):17.6 mg g^{-1}) through additional removal of those ions by Ni(II)-As(V) complexation. The overall results demonstrated CO_2-assisted pyrolysis can provide a viable platform to convert waste materials into fuel gases and environmental media for co-adsorption of cationic and anionic heavy metals.

KEYWORDS: *Fe-biochar composite; Pyrolysis; Arsenic; Nickel; Adsorption*

1. Introduction

Heavy metal pollution, mainly originating from industrial effluents from the mining and smelting activities, has become one of the critical issues worldwide due to its potential threat on human health and the environment (Jacob et al., 2018). Among the common toxic heavy metals (*e.g.*, As, Ni, Cd, Cr, and Mn, *etc.*), arsenic (As) contamination is of a serious concern in many parts of the world, especially in underdeveloped countries with limited financial and technology resources. Arsenic in aqueous phase occurs as two species with different oxidation state (*i.e.*, As(V) and As(III)), with the former prevalent in surface waters and the latter in groundwater. Ingestion of As species can cause acute/chronic damages to liver, lung, skin, cancer, and heart disease (Beck et al., 2018; Shakya et al., 2019). Nickel (Ni) exists in water in the form of Ni(II), and direct exposure to Ni(II) can lead to allergies and cancer (Erol and Özdemir, 2016). A few cases with water contamination by As(V) and Ni(II) in mining sites (Affandi and Ishak, 2019), landfill leachate (Öman and Junestedt, 2008), and industrial wastewaters (Li et al., 2017c) have been recently reported. In addition, the co-occurrence of As(V) and Ni(II) have been found in soil/groundwater nearby coal-fired power plants with relatively high concentration level (ppm level) (Deng et al., 2018). Therefore, there is a growing demand for efficient methods to eliminate As(V) and Ni(II) at the same time.

Remediation of wastewater containing As(V) and Ni(II) mainly involves the physicochemical reactions. The removal techniques of As(V) and Ni(II) included coagulation and precipitation (Akcil et al., 2015; Ihsanullah et al., 2016), adsorption (Akcil et al., 2015; Kheirandish et al., 2017), ion-exchange (Khan et al., 2019), filtration (Kumar et al., 2019), reverse osmosis (Ihsanullah et al., 2016), and membrane separation (Nasir et al., 2018). Among these techniques, adsorption process has been accepted as a viable option to remove As(V) and Ni(II) due to its technical simplicity and economic viability (Xu et al., 2018; Yang et al., 2017). A great deal of researchers has developed a variety of adsorbents (*e.g.*, modified zeolite, iron oxide-impregnated activated carbon, MOFs, polymeric composite *etc.*) suitable for the selective

removal of As(V) and Ni(II) from wastewater in the last decades (Al-Kaabi et al., 2019; Li et al., 2018; Ray and Shipley, 2015; Soni and Shukla, 2019). However, most adsorbents inevitably require one-sided input of energy for the material synthesis or the additional use of chemical reagents to establish the desired structure in composite matrix, which motivates the development of less energy-intensive and environmentally benign ways to produce adsorbent for As(V) and Ni(II) removal in a one-step process.

Biochar generated from thermal degradation (*i.e.*, pyrolysis) of biowaste has recently emerged as a new carbonaceous medium capable of removing various types of pollutants (*e.g.*, dye, herbicides, oil effluent, and heavy metal *etc.*) from water (Dawood et al., 2017; Li et al., 2017a; Liu et al., 2017). One of the advantages of biochar is that it can be fabricated using a variety of waste feedstocks including animal matter, wood waste, agricultural waste, food waste, sewage sludge, and manufacturing waste. Among these feedstocks, orange peel (OP) is generated as by-product of about 7 million tons each year, and its utilization as composting material is not appropriate due to its acidity (Siles et al., 2016). Thus, the alternative application of OP needs to be considered, and biochar precursor can be one of the viable options when considering the high fraction of organic substance in OP. Furthermore, the adsorption functionality of biochar has been further improved by surface modification using transition metal ions (Fe, Al, and Co) precipitation or co-pyrolysis with metal oxide (Li et al., 2017a; Sizmur et al., 2017). Given this favorable effect of transition metals addition, materials containing transition metal oxides can be considered as a candidate of surface modifier for biochar. Red mud (RM), one of the industrial by-products, contains a variety of transition metal oxides (*e.g.*, Fe, Al, and Si *etc.*). Unlike the unilateral energy consumption for thermal treatment in the synthesis of other adsorbents, biochar fabrication offers another merit of producing energy resources (*i.e.*, pyrolysis oil and syngas) during the pyrolytic process, which can compensate for the energy used by its operation. Compared to the common pyrolysis process using N_2 or Ar as feeding gas, employing CO_2 as reaction medium has led to the substantial generation of syngas (especially CO) through the enhanced cracking of VOCs via thermal breakdown of feedstock (Shen et al., 2017). With the incorporation of transition metal oxide into CO_2 pyrolysis, liquid/gaseous

products properties have been modified, thereby increasing the economic feasibility of the process (Tripathi et al., 2016).

Our recent work has reported the enhancement of syngas (especially CO) from CO_2 pyrolysis of OP through RM addition, and the produced CO was converted into H_2 via water-gas-shift reaction (Yoon et al., 2019). In this respect, it is highly desirable to use CO_2 as feeding gas in co-pyrolysis with RM in terms of fuel gas production.

However, it has not yet been disclosed which pyrolysis process is more suitable for the fabrication of biochar as an adsorbent. Moreover, most literature have dealt with the adsorption test in single adsorption system in which only one species of heavy metal exists. Given the potential diversity of heavy metal species detected in wastewater, the adsorption performance needs to be evaluated in multiple adsorption system containing more than one heavy metal ions. In addition, a new recipe for adsorbent synthesis that can co-adsorb As(V) and Ni(II) without any commercial chemical use needs to be developed. In this work, the adsorption ability of RM-derived biochar generated in N_2 and CO_2 environments was investigated in single- and binary adsorption systems of As(V) and Ni(II). Prior to the adsorption, the physicochemical properties of two OP biochar and two Fe-biochar composites were characterized with thermogravimetric (TGA) and spectroscopic instruments. The adsorption performance of Fe-biochar composites was evaluated under varying experimental conditions including solution pH, contact time, and initial concentrations.

2. Materials and methods

2.1. Sample preparation and chemical reagents

The OP was obtained from a local market in Republic of Korea, and RM (residue waste produced during alumina production) was provided from the Korea Institute of Geoscience and Mineral Resources (KIGAM, Daejeon, Republic of Korea). The elemental composition of OP included C (44 wt.%), H (6 wt.%), N (0.5 wt.%), S (0.6 wt.%), and O (0.5 wt.%), and RM consisted of Fe (37 wt.%), Al (23 wt.%), Si

(17 wt.%), Na (12 wt.%), Ti (8 wt.%), and Ca (3 wt.%) (Yoon et al., 2019). The feedstocks were physically crushed using a ball mill (PULVERISETTE 0, Fritsch, Germany), and then sieved using a 300-mesh screen (0.05 mm). Prior to the experiment, the feedstock samples were dried in the oven at 90 ˚C for 1 day to remove the moisture, and then placed in the desiccator at room temperature (20 ˚C±2). A mixture of OP and RM was equally homogenized using a mortar. Ultra-high purity (UHP, ≥ 99.9 %) grade N_2 and CO_2 gases were purchased from Green Gas Co. (Republic of Korea). Sodium arsenate dibasic heptahydrate ($Na_2HAsO_4 \cdot 7H_2O$, ≥98%) (Lot # BCBM0939V) and nickel(II) nitrate hexahydrate ($Ni(NO_3)_2 \cdot 6H_2O$) (Lot # N0024QH1) were obtained from Sigma-Aldrich (St. Lois, USA) and Daejung Chemical (Republic of Korea), respectively. Inductively coupled plasma (ICP) multi-element standard solution XVI with 21 elements (100 mg L^{-1} of As, Cd, Ca, Cr, Cu, Fe, Pb, Mg, Mn, Ni, and Zn, *etc.*) in diluted 6% nitric acid (Lot # HC60097287) was provided from Merck KGaA Co. (Darmstadt, Germany).

2.2. *Major pyrolytic gas analysis and preparation of Fe-biochar composite*

Pyrolytic gas measurement was conducted using two samples (*i.e.*, OP and OP/RM mixture) to investigate the influence of RM on syngas production. The mixture was mixed at equivalent mass ratio (*i.e.*, 1 g OP and 1 g RM). Samples of 2 ± 0.01 g was loaded in the center of set tubular reactor (TR). The detailed configuration of the TR was the same as that used in the previous study. (Yoon et al., 2019). The pyrolytic process was conducted at a heating rate 10 ˚C min^{-1} from 120 to 660 ˚C by injecting N_2 or CO_2 gases inside the TR, and the gas flow rate was controlled at 200 mL min^{-1} by mass flow controllers (MFCs). The accumulated amounts of major pyrolytic gases (*i.e.*, H_2, CH_4, and CO) were calculated after the analysis by a micro-gas chromatography (3000 Micro-GC, INFICON, Switzerland). When the pyrolytic processes were terminated, the TR was cooled down and the Fe-biochar composite were collected and then stored in a desiccator at room temperature. The Fe-biochar composite produced in N_2 and CO_2 environments were denoted as Fe-C-N_2 and Fe-C-CO_2, respectively.

2.3. Characterization of Fe-biochar composite

The characterization of Fe-biochar composites (Fe-C-N$_2$ and Fe-C-CO$_2$) was conducted with a series of instruments. In brief, the mass fractions of structured carbon and metal oxides in the Fe-biochar composite was estimated with TGA analysis (STA 499 F5 Jupiter, Netzsch, Germany). The surface morphology and elemental distribution of Fe-biochar composite were explored using a field emission scanning electron microscope and energy dispersive X-ray analyzer (FE-SEM/EDX) (Hitachi SU-8010, Japan). The mineralogical phase transformation during heating was examined using the X-ray diffractometer (XRD) (D8 Advance, Bruker-AXS, USA). The Fourier-transform infrared spectroscopy (FT-IR) was performed to examine which surface functional groups in the Fe-biochar composite were responsible for the adsorption of As(V) and Ni(II) using the Spectrum 100 (Perkin Elmer, USA). In addition, X-ray photoelectron spectroscopy (XPS) was used to explore the changes of peak distributions with binding energy in each surface element after the adsorption.

2.4. Adsorption of As(V) and Ni(II) by Fe-biochar composite adsorbents

All the adsorption experiments were conducted using 20 mL high density polyethylene (HDPE) (Fisher Scientific, USA) scintillation vials with the HDPE caps in duplicate at room temperature (20 ± 2 ℃). The pH of As(V) and Ni(II) solution was adjusted with 1 N HNO$_3$ and NaOH solutions. For the pH effect experiments, 0.02 g of Fe-biochar composite was added respectively into 20 mL of the solutions containing 20.3 mg L^{-1} As(V) or Ni(II) in single modes and 23.0 mg L^{-1} As(V) and 21.9 mg L^{-1} Ni(II) in binary modes, and the suspensions were agitated for 6 h. The adsorption kinetic experiments were performed for 24 h under the conditions of 1 g L^{-1} Fe-biochar composite and 21.6 mg L^{-1} As(V) or 21.5 mg L^{-1} Ni(II) (single mode) and 21.6 mg L^{-1} As(V) and 21.5 mg L^{-1} Ni(II) (binary mode). The adsorption isotherm experiments were conducted in two separate conditions. The first isotherm experiment was conducted by reacting 1 g L^{-1} Fe-biochar composite with the solutions containing the constant concentration of 19.8 mg L^{-1} Ni(II) and varying concentrations of 22.2-232.4 mg L^{-1} As(V) for 24 h. The

other experiment employed the constant concentration of 22.4 mg L^{-1} As(V) and varying concentrations of 21.7-218.5 mg L^{-1} Ni(II) at the same dose of Fe-biochar composite. To explore the adsorption selectivity of Fe-biochar composites for As(V) and Ni(II), the competitive ions effect experiments were carried out by using the anionic (PO_4^{3-}, NO_3^-, and Cl^-)/cationic ions [Cu(II), Cd(II), and Co(II)]. The competitive ions effect experiments of anionic ions on the adsorption of As(V) were conducted by injecting 1 g L^{-1} Fe-C-CO_2 into 21.8 mg L^{-1} As(V) solutions containing 20 mg L^{-1} of PO_4^{3-}, NO_3^-, and Cl^-, respectively. The effects of cationic ions on the Ni adsorption was studied by reacting the same dose (1 g L^{-1}) of Fe-C-CO_2 with 20.4 mg L^{-1} Ni(II) solutions containing 20 mg L^{-1} Cu(II), Cd(II), and Co(II), respectively. The adsorption proceeded for 24 h, and then the residual concentrations of As(V) and Ni(II) were measured after the filtration. The reusability experiments were performed in three repetitive cycles by repeating the adsorption/desorption reactions. The mixture solution containing 5.4 mg L^{-1} As(V) and 5.0 mg L^{-1} Ni(II) was used as initial solution. The adsorption occurred in the presence of 40 g L^{-1} Fe-C-CO_2 for 24 h, and the desorption was induced by 1 N NaOH solution spiking for 24 h. This cycle was repetitively performed up to 5 times. For all the adsorption experiments, the reactors containing solutions and adsorbents were shaken at 200 rpm with a water bath shaker (WiseShake SHO-1D, DAEHAN Scientific, Republic of Korea), and the reacted samples were filtered with 0.45 µm PVDF syringe filter (Whatman, USA) prior to the analysis. The concentration of mixed solution with As(V) and Ni(II) was analyzed using an inductively coupled plasma-optical emission spectrometry (ICP-OES) (Optima 5300 DV, Perkin Elmer, USA). The adsorbed amounts at equilibrium (q_e) were calculated q_e (mg g^{-1}) = ((C_0–C_e)·V)/W, where C_0 and C_e are initial and equilibrium concentration of adsorbates (mg L^{-1}), respectively, where V is the volume of mixed solution (L), and W is the dry mass of adsorbent (g).

2.5. Data analysis

The adsorption data obtained from the kinetics experiments were modeled by using the pseudo-first-order (PFO), pseudo-second-order (PSO), and intra-particle diffusion (IPD) kinetic models. In addition,

the data from adsorption isotherm experiments were fitted with the Langmuir and Freundlich isotherm models. The details of modeling procedure are presented in Supplementary materials.

3. Results and discussion

3.1. Gas measurement from co-pyrolysis in N_2 and CO_2

The production of gaseous products (H_2, CH_4, and CO) from pyrolysis processes (1 g OP & 1 g OP/1 g RM) in N_2 and CO_2 environments were characterized to compare their evolution patterns, and the results were presented in Fig. S1.

As shown in Fig. S1 (a), the accumulation of major pyrolytic gases generated from the pyrolysis of OP was different in N_2 and CO_2 environment. The cumulative concentrations of H_2 were 3.9 and 1.9 mole % in N_2 and CO_2 environment, respectively, which could be attributed to the more consumption of H_2 by CO_2 hydrogenation through reverse water-gas shift reaction ($CO_2 + H_2 \rightarrow CO + H_2O$) (Daza et al., 2014). The generation patterns of CH_4 in both environments were almost similar, accounting for 1.9 and 1.5 mole % in N_2 and CO_2 environment, respectively. On the other hand, there was a remarkable difference in CO accumulation between N_2 (3.3 mole %) and CO_2 (6.9 mole %) environment. The enhancement of CO evolution in the presence of CO_2 can be explained by the homogeneous reaction of CO_2 and volatile organic carbons (VOCs) (Lee et al., 2017). The thermal breakdown of VOCs promoted by CO_2 (*i.e.*, thermal CO_2-activation) probably led to the increased release of carbon-containing gases including CO. This effect was further enhanced when co-pyrolyzing RM and OP, with the cumulative concentrations of CO being 4.3 mole % for N_2 and 17.7 mole % for CO_2 (Fig. S1 (b)). This observation is likely due to the catalytic effect of Fe mineral phases in RM, which enhanced the breakdown of hydrocarbons during heating (Li et al., 2016).

3.2. Physicochemical characteristics of Fe-biochar composite

TGA tests were conducted in air condition to investigate the mass loss of Fe-biochar composite and identify the mass fractions of carbonaceous materials and metal oxides, and the results were presented in Fig. 1. The thermal treatment of RM up to 900 °C resulted in the reduction in mass weight by 16.7 wt.%, which could be due to thermal destruction of OH^-, H^-, and O bonds in the RM (do Prado et al., 2017; Nath et al., 2015). For OP biochar, the substantial reduction of mass weight (85.1 wt.% reduction for N_2 and 84.2 wt.% reduction for CO_2) in the temperature range of 35-900 °C was observed. For Fe-biochar composite, there was a relatively lower loss in mass weight of Fe-C-CO_2 (26.2 wt.%) and Fe-C-N_2 (31.6 wt.%), indicating lower carbon content in the former. This is another evidence of enhanced thermal breakdown of carbon sources in OP by CO_2 during pyrolysis, which is further catalyzed by the presence of RM.
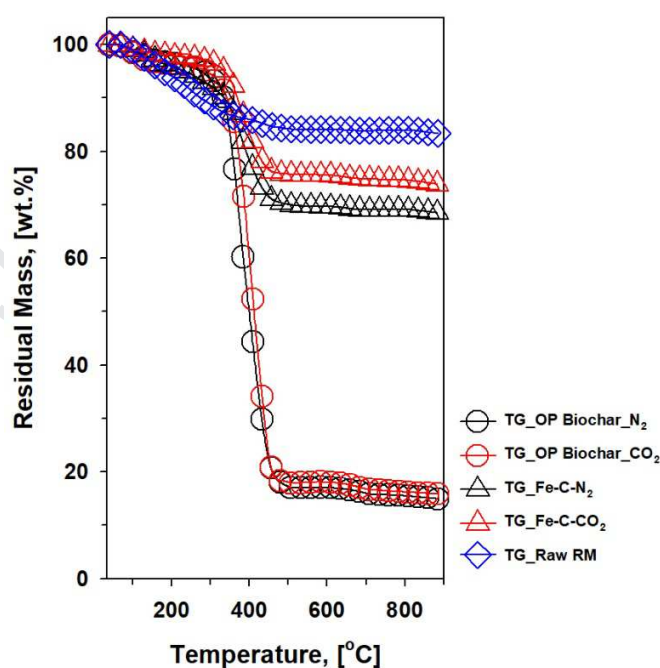

Fig. 1. TGA analysis of OP biochar, Fe-biochar composite, and RM (sample dose: 10 ± 0.01 mg, inert gas: air, gas flow rate: 70 mL min^{-1}, temperature range: 35-900 °C, and heating rate: 10 °C min^{-1})

The results of FE-SEM/EDX analysis of OP biochar and Fe-biochar composite were shown in Fig. 2. As shown in Fig. 2 (a), (b), surface morphologies of two OP biochar samples produced in N_2 and CO_2 environments were similar to each other as well as their elemental composition (Fe-C-N_2: 91.6 wt.% C and 5.9 wt.% O, Fe-C-CO_2: 92.9 wt.% C and 5.8 wt.% O). Likewise, no morphological difference was revealed in Fe-C-CO_2 and Fe-C-N_2 (Fig. 2 (c), (d)). However, Fe-C-CO_2 showed the lower C content (40.8 wt.%) and the higher O content (47.3 wt.%) than those of Fe-C-N_2 (C: 80.1 wt.%, O: 17.8 wt.%), which is consistent with the less carbon content in Fe-C-CO_2 revealed in TGA test.
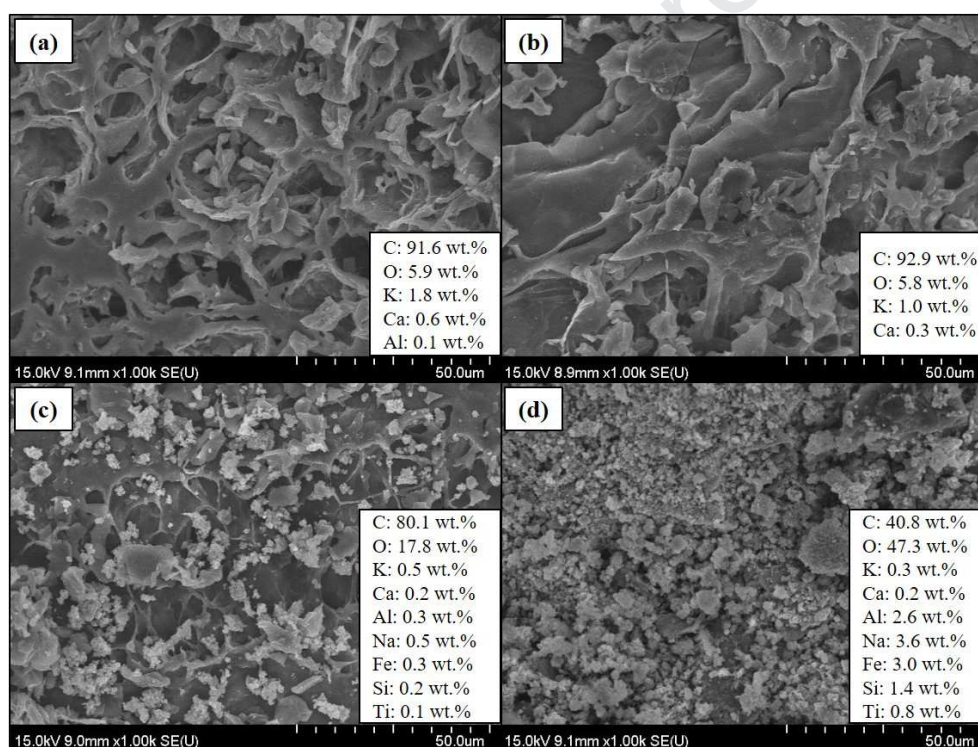

Fig. 2. FE-SEM/EDX data of OP biochar generated in (a) N_2 and (b) CO_2 environments and (c) Fe-C-N_2 and (d) Fe-C-CO_2

The results of XRD analysis of Fe-biochar composite were shown in Fig. 3. Red mud contained hematite (α-Fe_2O_3, JCPDS No. 73-2234) as a major Fe phase (Cho et al., 2019; Feng et al., 2016), but it disappeared during pyrolysis and new Fe phases were created in two Fe-biochar composites. For example,

the main Fe product of both Fe-C-N_2 and Fe-C-CO_2 was found to be magnetite (Fe_3O_4, JCPDS No. 19-0629) (Xu et al., 2019). These observations can be explained by the reduction of hematite to magnetite through the thermochemical reaction between OP and RM (Cho et al., 2019). In addition, metallic Fe phase (Fe^0, JCPDS No. 01-1252) was exclusively formed in Fe-C-N_2 (Gong et al., 2016; Sun et al., 2019). Despite the more enhanced conversion of hydrocarbons to gases in CO_2 environment, Fe^0 was not produced in Fe-C-CO_2, presumably due to other preferential redox reactions involving CO_2 to form different Fe products (*e.g.*, $CO_2 + 3FeO \rightarrow CO + Fe_3O_4$) (Di et al., 2019). This observation has practical implication in biochar application because adsorption ability and functionality of biochar are greatly influenced by the type of Fe solid.
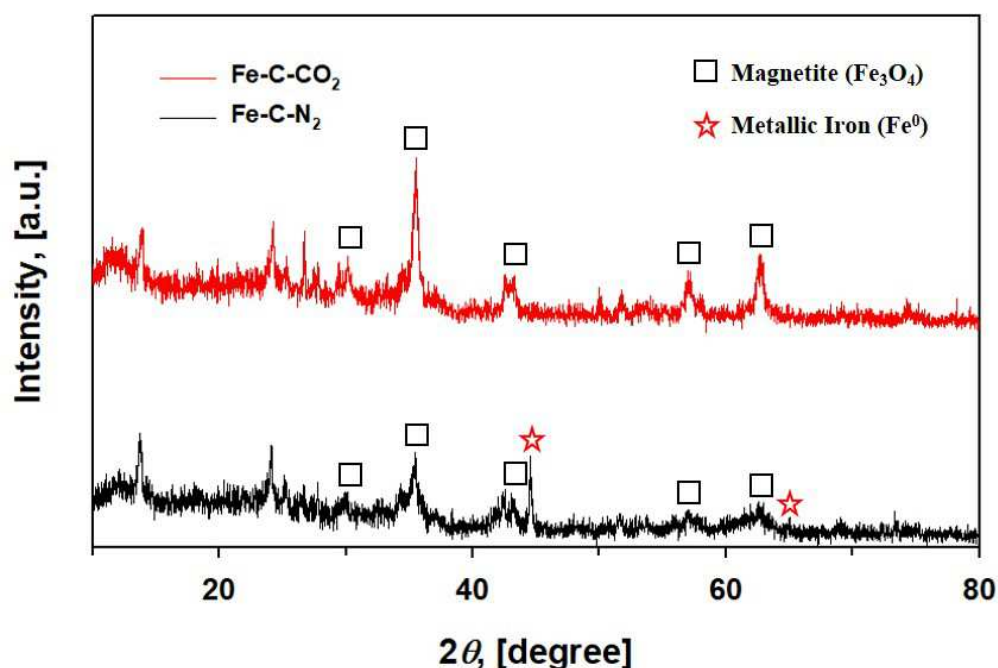

Fig. 3. XRD patterns of Fe-C-N_2 (black) and Fe-C-CO_2 (red)

To explain the syngas enhancement in the presence of CO_2, the porous structure of Fe-biochar

composites has been characterized in our previous work that has studied catalytic pyrolysis mechanism enhancing H_2 production and CO_2 looping reaction (Yoon et al., 2019). These Fe-biochar composites showed the similar values of BET surface area (Fe-C-N_2: 46.44 m^2 g^{-1}, Fe-C-CO_2: 44.22 m^2 g^{-1}) and total pore volumes (Fe-C-N_2: 0.09 cm^3 g^{-1}, Fe-C-CO_2: 0.1 cm^3 g^{-1}) (Fig. S2). The hysteresis curves observed at 0.5-0.9 P/P$_0$ indicates that these materials also possess a large amount of mesopores. These results suggest mixing the material containing metal oxides (*i.e.*, RM) with biomass feedstock in pyrolytic process is very effective to induce the creation of well-developed porous structure in the biochar matrix.

FT-IR analysis of the reacted Fe-C-CO_2 was carried out and the results were presented in Fig. S3. The FT-IR spectrum of Fe-C-CO_2 showed the profile of surface functional groups present in typical carbonaceous material with several peaks assigned to O-H (976 cm^{-1}), C-O (1087 cm^{-1}), -CH_2 (1436 cm^{-1}), and -OH (1574 cm^{-1}) (Bian et al., 2019; Jiang et al., 2019). A peak for -CH_2 (1438 cm^{-1}) disappeared after the adsorption reaction, which might be due to the binding of metal ions to carbon functional groups (Shen et al., 2019). Another peak for M-O (metal-oxygen) or M-O-M (849 cm^{-1}) was newly formed in multiple mode (Huang et al., 2018; Li et al., 2017b). This profile variation supports Ni(II)-As(V) complex formation on the surface of Fe-biochar composite (Liu et al., 2015b; Wang et al., 2016).

3.3. Effect of pH on the adsorption of As(V) and Ni(II)

The effect of solution pH on the adsorption behavior of As(V) and Ni(II) by Fe-C-N_2 and Fe-C-CO_2 was investigated. Adsorption of As(V) and Ni(II) showed great dependence on solution pH for both Fe-biochar composite (Fig. 4 (a),(b)). The adsorption of As(V) increased with the increase of final pH from 3.0 to 5.8. The lower adsorption of As(V) at low pH may be related to dissolution of magnetite/Fe^0 at highly acidic condition (initial pH 2), leading to elimination of the adsorption sites for As(V) in the Fe-biochar composite. At pH > 5.8, adsorption of As(V) linearly decreased from 20.1 mg g^{-1} (Fe-C-N_2) and 18.7 mg g^{-1} (Fe-C-CO_2) to around 0.8 mg g^{-1} when the final pH increased from 5.8 to 10. This is attributable to increased electrostatic repulsion between anionic As(V) ions and magnetite (pH$_{pzc}$ = 8.0)

and Fe^0 (pH_{pzc} = 7.8) with a pH increase (Sigdel et al., 2016; Tanboonchuy et al., 2011). Another possibility is that the increased number of OH^- ions at alkaline pH condition could interfere with As(V) adsorption due to the competitive effect for the adsorption sites (Inchaurrondo et al., 2019). For Ni(II) adsorption, the acidic pH condition resulted in less removal of Ni(II), while the adsorption increased as the final pH increased up to 9. At low pH, strong electrostatic repulsion between cationic Ni(II) and positively charged surfaces of the Fe-biochar composite (*i.e.*, protonated functional groups) could substantially decrease the adsorption efficiency. On the other hand, adsorption of Ni(II) becomes more favorable at high pH condition with the increase of negative charge density on the surface. In addition, electrostatic attraction surface precipitation of $Ni(OH)_2$ might contribute to the removal of Ni(II) at alkaline pH condition.

To explore the pH-dependent adsorption of As(V) and Ni(II) when they are present together, experiments were conducted using a mixed solution containing 23.0 mg L^{-1} As(V) and 21.9 mg L^{-1} Ni(II). The most notable difference between single- and binary adsorption experiments was the adsorption of As(V) in the alkaline pH (> final pH 7.3) (Fig. 4 (c)). In contrast to the sharp decrease of As(V) adsorption to 0.8 mg g^{-1} in the single adsorption experiment, the adsorption was maintained at approximately 10 mg g^{-1} in the binary adsorption experiment. This observation suggests that another site of adsorption became active to remove As(V). Adsorption of Ni(II) in the binary mode followed a similar pattern as that in the single mode (Fig. 4 (d)), which indicates that Ni(II) adsorption behavior was not affected by the presence of As(V). Considering that there was little increase of Ni(II) adsorption in the presence of As(V), the enhanced adsorption of As(V) in the presence of Ni(II) adsorption likely occurred by surface complexation of Ni(II)-As(V) rather than Ni(II)-As(V) co-precipitation.
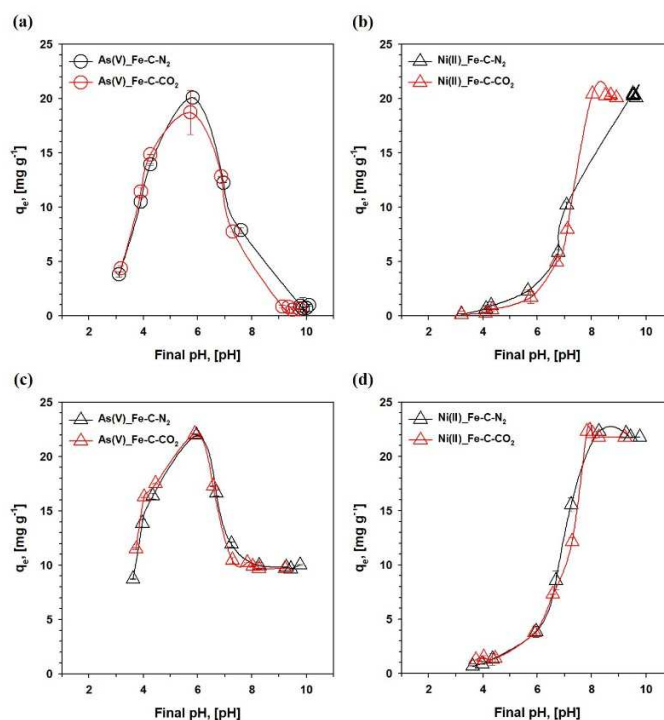
Fig. 4. Effect of solution pH on the (a) As(V) or (b) Ni(II) single adsorption and the (c) As(V) and (d) Ni(II) binary adsorption by Fe-C-N$_2$ (black) and Fe-C-CO$_2$ (red) (sample dose: 1 g L^{-1}, initial single concentration: 20.3 mg L^{-1} As(V) or Ni(II), initial mixed concentration: 23.0 mg L^{-1} As(V) and 21.9 mg L^{-1} Ni(II), final pH: 3.1-10.1, contact time: 6 h)

3.4. As(V) and Ni(II) adsorption kinetics in single- and binary modes

Adsorption kinetics experiments were carried out in single and binary modes. In single mode, As(V) adsorption on the two Fe-biochar composites steadily increased within 240 min (Fe-C-N$_2$: 7.5 mg g^{-1}, Fe-C-CO$_2$: 5.6 mg g^{-1}), followed by slight decreases to 5.7 mg g^{-1} for Fe-C-N$_2$ and 5.3 mg g^{-1} for Fe-C-CO$_2$ at 1,400 min (Fig. 5 (a),(b)). The reduction in As(V) adsorption is ascribable to the increase in solution pH (pH 7.5 → pH 8) occurred in later reaction time. The alkaline property of the Fe-biochar composite continued to alter the suspension pH after the initial adsorption was completed, leading to desorption of As(V) to some extent. For Ni(II) adsorption, the adsorption proceeded slowly and gradually to yield 16.2 mg g^{-1} in Fe-C-N$_2$ and 15.1 mg g^{-1} in Fe-C-CO$_2$ during 1,400 min (Fig. 5 (c), (d)). This different adsorption kinetics between As(V) and Ni(II) adsorption implies the adsorption of As(V) and Ni(II) involves different adsorption sites on the Fe-biochar composite. The relatively faster adsorption of As(V)

suggests that the adsorption sites were mainly present on the outer surface of Fe-biochar composite (*i.e.*, RM-derived oxides embedded in the carbon matrix), whereas adsorption via pore diffusion through carbon pores played an important role in Ni(II) adsorption, resulting in slower but continuous adsorption of Ni(II) over the whole reaction time (Kołodyńska et al., 2017). In addition, hydrolysis of Ni(II) sorbed onto the Fe-biochar composite might suppress the increase in suspension pH, which showed a lower pH value (below pH 7.2) compared to As(V) adsorption (Fig. S4 in Supplementary Materials). The experimental adsorption capacities (q_e (exp.)) of As(V) and Ni(II) by the two adsorbents (Fe-C-N_2 and Fe-C-CO_2) were close to the calculated adsorption capacities of the PSO model (q_e (cal.)), as well as the correlation coefficients (R^2) of the PSO model was higher than the PFO model (Table 1). These suggest the importance of chemisorption in adsorption of As(V) and Ni(II) (Kołodyńska et al., 2017; Wu et al., 2018).
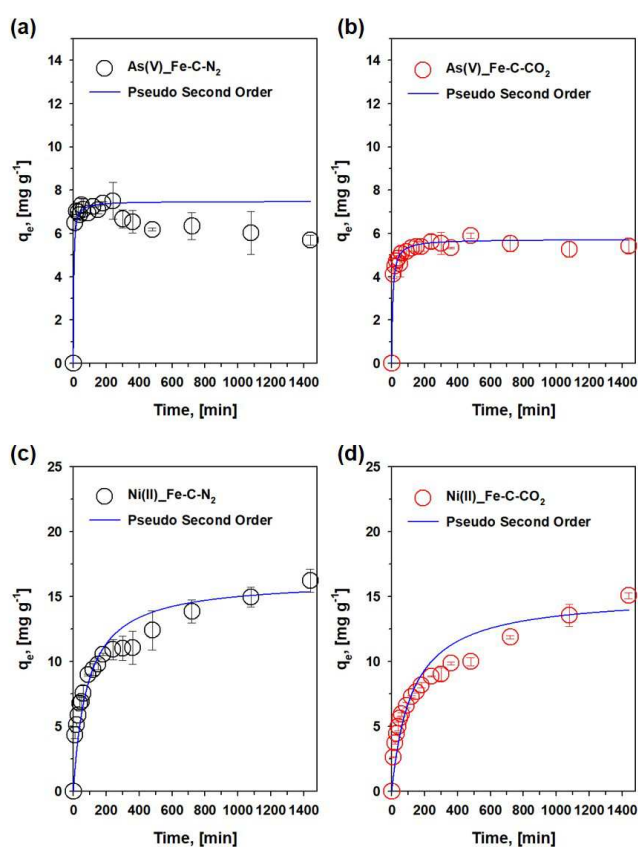

Fig. 5. Adsorption kinetics of As(V) by (a, c) Fe-C-N_2 and (b, d) Fe-C-CO_2 in single mode (sample dose:

1 g L^{-1}, initial concentration: 21.5 mg L^{-1} As(V) and 21.7 mg L^{-1} Ni(II), final pH: 7.2-8.1, contact time: 0-1440 min)

Table 1. Adsorption kinetics model parameters of PFO and PSO for the adsorption of As(V) and Ni(II) by Fe-biochar composite**s** in single and binary model

System	Adsorbent	Adsorbate	q$_e$, (exp.) [mg g^{-1}]	PFO Kinetics Model			PSO Kinetics Model		
				k$_1$ [L min^{-1}]	q$_e$, (cal.) [mg g^{-1}]	R^2 [-]	k$_2$ [g mg^{-1} min^{-1}]	q$_e$, (cal.) [mg g^{-1}]	R^2 [-]
Single	**Fe-C-N$_2$**	**As(V)**	7.5	0.0074	0.68	0.4701	0.0444	7.48	0.9988
		Ni(II)	16.2	0.0021	9.78	0.9612	0.0007	16.29	0.9881
	Fe-C-CO$_2$	**As(V)**	5.6	0.0111	1.35	0.9262	0.0249	5.69	0.9987
		Ni(II)	15.1	0.0018	10.53	0.9717	0.0005	15.15	0.9757
Binary	**Fe-C-N$_2$**	**As(V)**	13.70	0.0016	5.73	0.8963	0.0014	13.40	0.9931
		Ni(II)	20.71	0.0021	14.43	0.9620	0.0004	21.28	0.9888
	Fe-C-CO$_2$	**As(V)**	13.35	0.0018	7.66	0.9724	0.0009	13.77	0.9875
		Ni(II)	17.61	0.0021	13.81	0.9777	0.0003	18.62	0.9852

Adsorption of As(V) and Ni(II) in binary mode showed different patterns from single mode. Unlike As(V) adsorption in single mode, the adsorption steadily increased over 1,400 min and yielded much enhanced q$_e$ values for both Fe-biochar composite (13.7 mg g^{-1} for Fe-C-N$_2$ and 13.4 mg g^{-1} for Fe-C-CO$_2$) (Fig. 6 (a), (c)). Desorption of As(V) observed in later reaction times in single mode experiment was not observed, which could be linked to stable pH condition maintained throughout the reaction time (Fig. S5 in Supplementary materials). In case of Ni(II), there was a slight enhancement of Ni(II) adsorption, but it was not as significant as As(V) adsorption (q$_e$ values of 20.7 mg g^{-1} for Fe-C-N$_2$ and 17.6 mg g^{-1} for Fe-C-CO$_2$) (Fig. 6 (b), (d)). The adsorption increases of both ions indicate that it is more advantageous to use the Fe-biochar composite in binary adsorption mode. As discussed earlier, the enhanced adsorption in binary mode is likely due, in part, to the formation of Ni(II)-As(V) complexes (Liu et al., 2015b). This complex formation may have occurred mainly on inner pore surfaces where Ni(II) binding preceded As(V) complexation, as indicated by relatively lower adsorption enhancement of Ni(II) as compared to As(V).
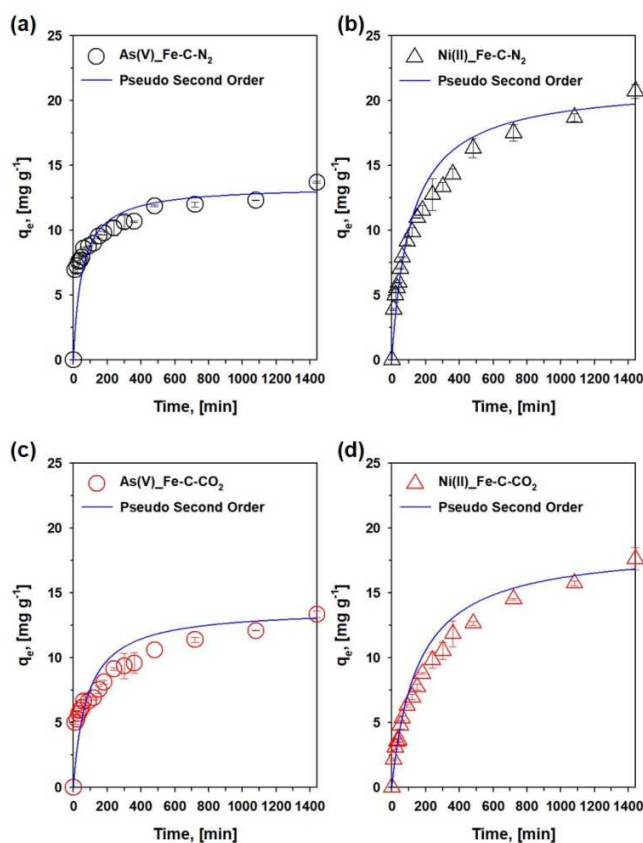
Fig. 6. Adsorption kinetics of As(V) and Ni(II) by (a, b) Fe-C-N$_2$ and (c, d) Fe-C-CO$_2$ in binary mode (sample dose: 1 g L^{-1}, initial mixed concentration: 21.7 mg L^{-1} As(V) and 21.3 mg L^{-1} Ni(II), final pH: 7.4, contact time: 0-1440 min)

The intraparticle diffusion (IPD) model was used to get more insights into the adsorption kinetics of As(V) and Ni(II) by Fe-C-N$_2$ and Fe-C-CO$_2$, and the fitting results and associated modeling parameters were presented in Fig. 7 and Table S1 in Supplementary materials, respectively. Based on the fitting data, the adsorption kinetics were divided into two adsorption steps. The 1st adsorption step commonly involves the adsorption occurring on the outer surfaces. In this regard, it is assumed that the initial adsorption of As(V) and Ni(II) proceeded relatively rapid by magnetite/Fe^0 embedded onto the external surfaces or carbon layers exposed to the outside of Fe-biochar composite (Liu et al., 2015a). The 2nd adsorption step indicates the adsorption occurring inside the Fe-biochar composite framework, requiring ion diffusion to the adsorption sites located on the inner surfaces. Thus, time to reach the adsorption equilibrium can significantly increases due to the slow diffusion process (Cho et al., 2016; Lu et al., 2017). The adsorption

of Ni(II) followed these multiple steps, but the 2nd adsorption step was not observed in the single adsorption experiment of As(V) adsorption. This result suggests that As(V) ions were mostly removed in the external surfaces of the Fe-biochar composite. However, the remarkable changes in K_{IPD} values for the 2nd As(V) adsorption step in the binary adsorption mode (Fe-C-N$_2$: -0.0405 → 0.1325 mg g^{-1} min$^{-0.5}$, Fe-C-CO$_2$: 0.0102 → 0.3300 mg g^{-1} min$^{-0.5}$) suggest that adsorption via the 2nd adsorption step also became important in the presence of Ni(II). This observation further supports removal of As(V) by forming Ni(II)-As(V) complexes within the inner pore surfaces of the Fe-biochar composite.
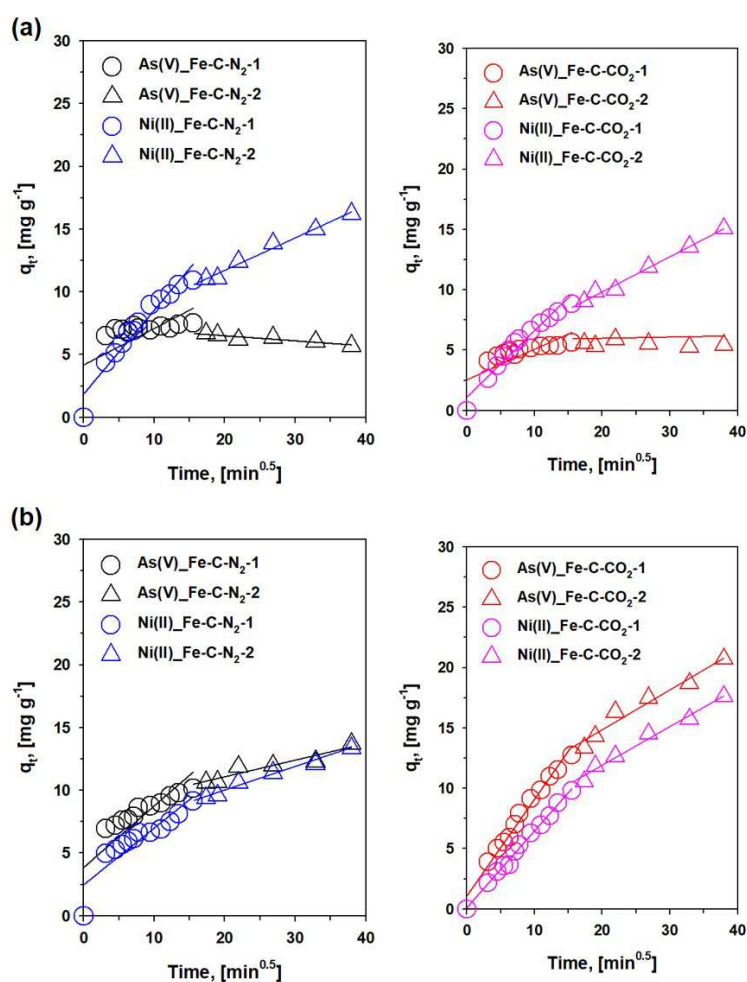

Fig. 7. Intraparticle diffusion (IPD) model fitting of As(V) and Ni(II) (a) single- and (b) binary adsorption systems (1st stage: ○ and 2nd stage: △)

3.5. Adsorption isotherm of As(V) and Ni(II)

Based on the adsorption kinetics results, the simultaneous removal of As(V) and Ni(II) was further studied by conducting adsorption isotherm experiments in binary adsorption mode. The adsorption isotherm experiments were conducted by varying 1) the initial concentration of As(V) from 22.2 to 232.4 mg L^{-1} at a fixed Ni(II) concentration of 21.7 mg L^{-1}, and 2) the initial concentration of Ni(II) from 21.7 to 218.5 mg L^{-1} at a fixed As(V) concentration of 22.4 mg L^{-1}. The experimental data was fitted with Langmuir and Freundlich isotherm models, and the modeling parameters were presented in Table S2 in Supplementary materials.

In first case, the maximum adsorption amount of As(V) at fixed Ni(II) concentration was slightly higher for Fe-C-CO$_2$ (37.4 mg g^{-1}) than Fe-C-N$_2$ (33.9 mg g^{-1}) (Fig. 8). This observation may be explained by the relative carbon content and distribution of iron oxides in the two Fe-biochar composites. As revealed in microscopic images of the Fe-biochar composite (Fig. 2 (c), (d)) and TGA results (Fig. 1), iron oxides are embedded on the structural carbon phase and carbon content is relatively less in Fe-C-CO$_2$. This would allow more facile access of As(V) to iron oxides that are presumed to play an important role in As(V) adsorption. In addition, the increase of initial concentration of As(V) resulted in a progressive decrease of Ni(II) adsorption for both Fe-biochar composite. This suggests As(V) and Ni(II) share a few adsorption sites and that adsorption of Ni(II) was inhibited by As(V), with its impact more significant at high As(V) concentrations.

In second case, the maximum adsorption amounts of Ni(II) at fixed As(V) concentration were found to be 35.7 and 33.0 mg g^{-1} for Fe-C-N$_2$ and Fe-C-CO$_2$, respectively (Fig. 9). The slightly higher adsorption of Ni(II) by Fe-C-N$_2$ signifies the importance of carbon phase in the adsorption process. Interestingly, adsorption of As(V) at varying concentration of Ni(II) showed an opposite tendency to show an increase with increasing Ni(II) concentration. This observation indicates the creation of new adsorption sites for As(V) provided by Ni(II) adsorption onto the Fe-biochar composite. The adsorption of As(V) showed negligible effect on the adsorption of Ni(II) at the condition that the initial As(V) concentration was
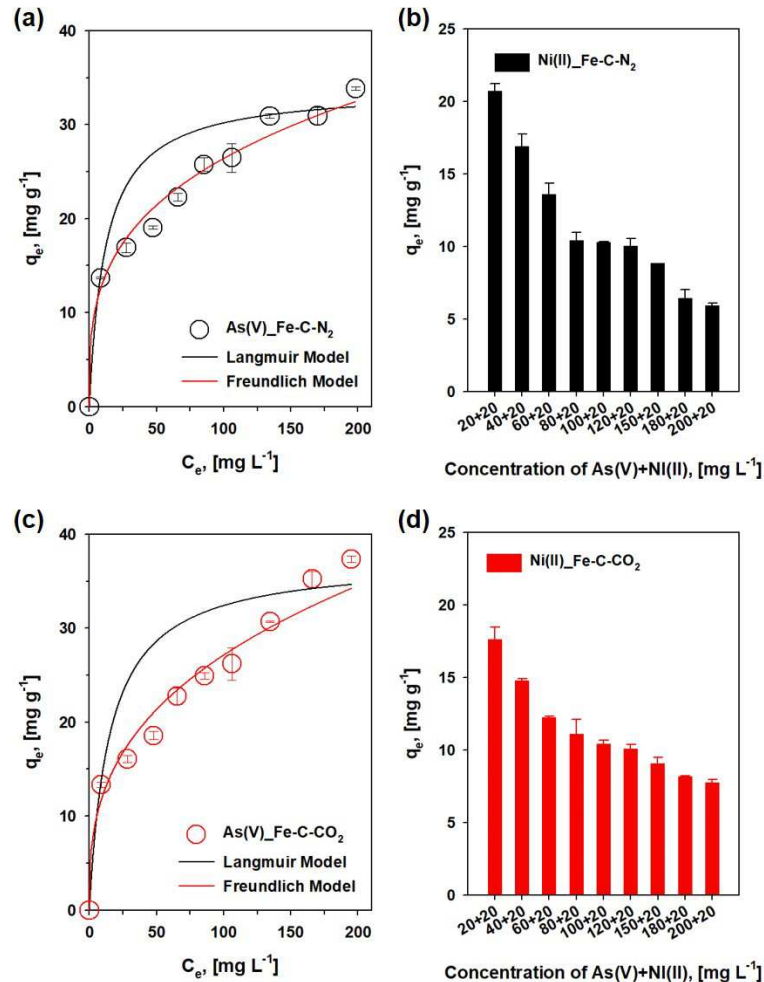
relatively low (20 mg L^{-1}).

Fig. 8. Adsorption isotherm of (a, c) As(V) and (b, d) Ni(II) by Fe-C-N$_2$ and Fe-C-CO$_2$ (sample dose: 1 g L^{-1}, initial mixed concentration: 22.2-232.4 mg L^{-1} As(V) and 21.7 mg L^{-1} Ni(II), final pH: 6.5, contact time: 24 h)

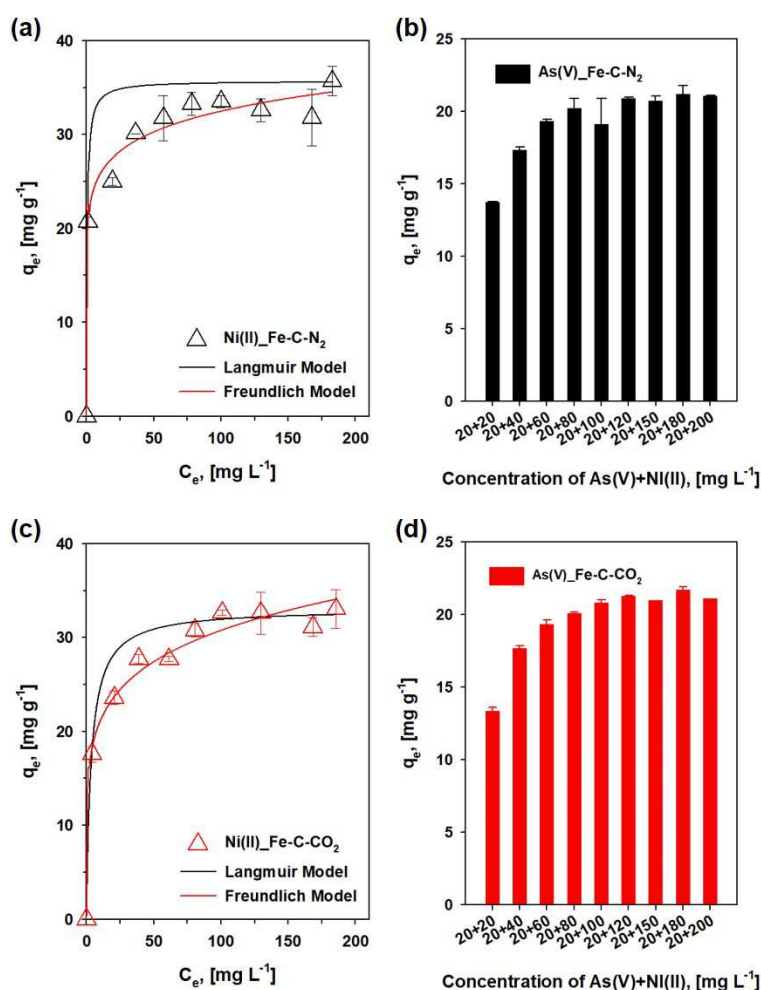**Fig. 9.** Adsorption isotherm of (a, c) Ni(II) and (b, d) As(V) by Fe-C-N_2 and Fe-C-CO_2 (sample dose: 1 g L^{-1}, initial mixed concentration: 21.7-218.5 mg L^{-1} Ni(II) and 22.4 mg L^{-1} As(V), final pH: 6.7, contact time: 24 h)

The parameters obtained from adsorption isotherm modeling are presented in Table S2 in Supplementary materials. The results indicated the Freundlich model better described the adsorption of As(V) and Ni(II) than the Langmuir model, suggesting that the Fe-biochar composite possess a variety of available adsorption sites distributed on one more type of host (*e.g.*, structured carbon and metal oxides) (Shen et al., 2019). In addition, The value of *n* higher than 3 in the Freundlich model (As(V): 3.32 and 2.88, Ni(II): 9.98 and 6.05 for Fe-C-N_2 and Fe-C-CO_2, respectively) also indicates that adsorption occurs on the heterogeneous surfaces with relatively strong bonding (Jemutai-Kimosop et al., 2020; Jeon et al., 2018).

3.6. co-adsorption mechanisms of As(V) and Ni(II)

Based on the adsorption results, co-adsorption mechanism of As(V) and Ni(II) in the presence of Fe-biochar can be described as shown in Fig. 10. In the single system, Ni(II) could be mainly bound to the surface functional groups as revealed in the FT-IR analysis (Fig. S3). Most of As(V) adsorption is presumed to occur on the Fe-oxide surfaces, and As(V) complexation with oxygen-containing functional groups (*i.e.*, C-OOH) may also occur but to a lesser extent. Adsorption of As(V) was significantly enhanced in the binary system when Ni(II) is present at fixed concentration of 20 mg L^{-1}. This enhancement is likely due to a multi-step process that involves initial biding of cationic Ni(II) on the functional groups, followed by subsequent binding of anionic As(V) in the form of Ni(II)-As(V) complex. Meanwhile, the progressive increase of As(V) concentration to 200 mg L^{-1} decreased Ni(II) adsorption (Fig. 8 (b),(d)), presumably due to the increased competition between As(V) and Ni(II) for common adsorption sites (functional groups). However, this competition effect was not observed when As(V) concentration was fixed at 20 mg L^{-1}, which suggests the common functional groups were not fully occupied by As(V), but could provide complexation sites for further Ni(II) adsorption.
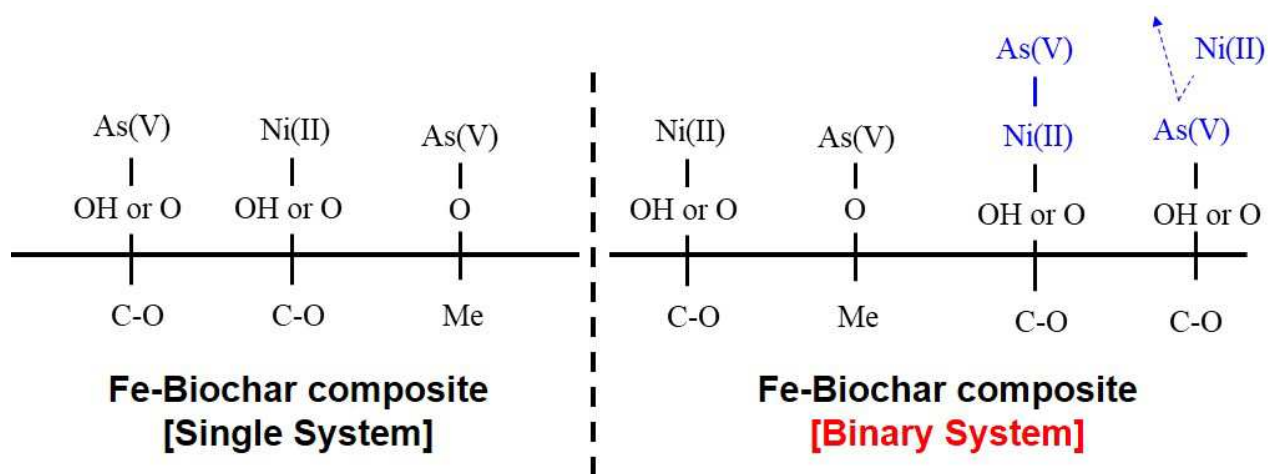

Fig. 10. A schematic diagram for possible adsorption reactions in single- and binary systems of As(V) and Ni(II)

3.7. Competitive ions effect and reusability of Fe-C-CO$_2$

The competitive ions effect on co-adsorption of As(V) and Ni(II) by CO$_2$C was studied and the results were presented in Fig. 11. Overall, the presence of anionic- or cationic ions at 20 mg L^{-1} negatively affected adsorption of As(V) and Ni(II). The removal efficiency of As(V) was found to be 60.1%, and the negative effect was in the order of PO$_4^{3-}$ (9.1%) > Cl$^-$ (42.4%) > NO$_3^-$ (52.7%) (Fig. 11 (a)). These results suggest that adsorption of PO$_4^{3-}$ onto Fe-biochar mainly occurs in a similar manner as As(V) (*i.e.* inner-sphere complexation) (Kumar and Jiang, 2016). Meanwhile, the adsorption of Ni(II) (81.2% removal efficiency) was little influenced by the presence of Cu(II) (81.1% removal efficiency), but it was more influenced by Cd(II) (56.3%) and Co(II) (28.1%) (Fig. 11 (b)). This apparent differences in their effects may be explained by their different ionic radius (Co(II): 0.65 Å, Ni(II): 0.69 Å, Cu(II): 0.73 Å, Cd(II): 0.87 Å) such that metal ions with smaller ionic radius are more readily adsorbed onto adsorption sites than those with bigger ionic radius (Long et al., 2020; Mahdi et al., 2018). Therefore, it is expected that the inhibition effect was greatest for Co(II) and least for Cd(II). However, Cd(II) had an apparent inhibition effect on Ni(II) adsorption although it has a bigger ionic radius than Ni(II). A similar observation has been found in is a previous work that studied the binary adsorption of Cd(II) and Ni(II) (Deng et al., 2019). They reported that the binary adsorption of Ni(II) in the presence of Cd(II) was inferior to the single adsorption of Ni(II), and suggested that adsorption competition between Cd(II) and Ni(II) inhibited the cation exchange mechanism by the functional groups of biochar.

The repetitive adsorption/desorption experiments with regenerated Fe-biochar were conducted, and the results were provided in Fig. S6. In the adsorption cycle, co-adsorption of As(V) and Ni(III) proceeded for 24 h. The regeneration of the biochar co-loaded with As(V) and Ni(II) is a challenging issue because two ions have opposite charges. The selected regeneration approach was to use 1 N NaOH solution to desorb As(V) ions sorbed onto Fe-biochar and to convert Ni(II) ions into Ni-oxide solid phase. The removal of As(V) was found to be 90.5% in the 1st adsorption cycle, but the efficiency significantly

dropped to 37.3-43.3% in the next cycles (~5th cycle). This reduction might be attributed to the strong alkaline condition of the biochar due to NaOH treatment. Successive NaOH treatments sharply increased the solution pH up to above 12 in the next cycles, and progressively decreased the adsorption efficiency of As(V) removal. Meanwhile, almost 100% removal of Ni(II) was achieved in all the cycles because of precipitation reaction under the strong alkaline pH condition created by the biochar. These observations suggest that the regeneration of Fe-biochar by NaOH treatment is a feasible option, however it inevitably results in substantial decrease in adsorption of anionic metal in the reuse step.
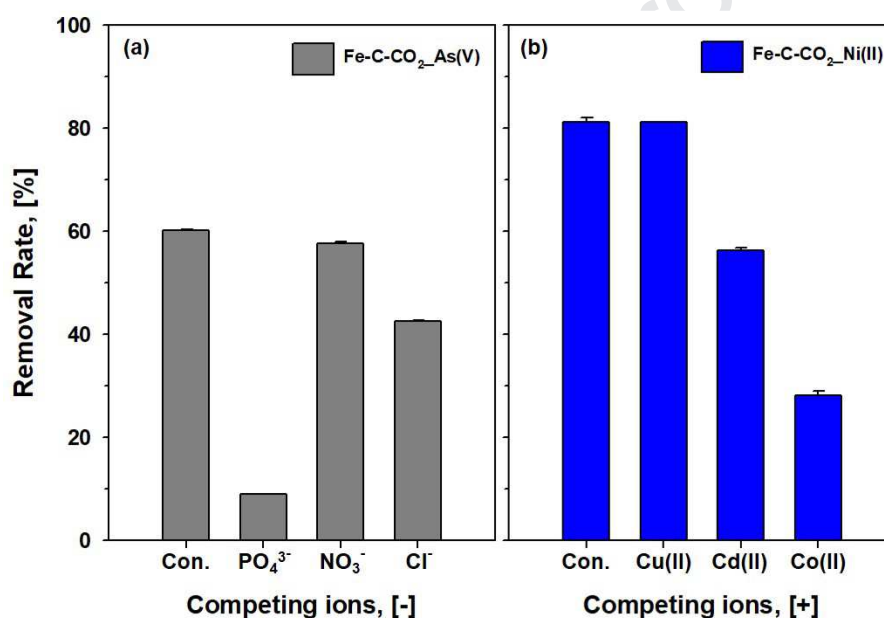

Fig. 11. Competitive ions effect of (a) As(V) and (b) Ni(II) by Fe-C-CO_2 (sample dose: 1 g L^{-1}, initial concentration: 21.8 mg L^{-1} As(V), 20.4 mg L^{-1} Ni(II), and 20 mg L^{-1} PO_4^{3-}, NO_3^-, Cl^-, Cu(II), Cd(II), Co(II), final pH: 6.6-7.8, contact time: 24 h)

4. Conclusions

In this work, Fe-biochar composite adsorbents were produced along with syngas generation through thermochemical conversion of orange peel with red mud in N_2 and CO_2 environments. In terms of syngas yield, injecting CO_2 as feeding gas was considered as more suitable option to produce more CO during pyrolysis. The Fe-biochar composite produced in two atmospheres contained different mineralogical Fe

phase (CO_2: only magnetite, N_2: magnetite and Fe^0). The adsorption performance of the two Fe-biochar composites was evaluated in single- and binary adsorption modes for adsorption of As(V) and Ni(II). In the single mode, the adsorption kinetics of As(V) reached equilibrium (240 min) relatively faster than that of Ni(II), but desorption of As(V) occurred at extended reaction time due to pH increase. The adsorption capacities of As(V) by the Fe-biochar composites were further enhanced in binary mode owing to Ni(II)-As(V) complex formation. Oppositely, the increase of As(V) concentration inhibited Ni(II) adsorption due to the competitive effect of As(V). In overall, two Fe-biochar composites possessed comparable adsorption performance for As(V) and Ni(II), and were suitable for simultaneous treatment of As(V) and Ni(II) in aqueous solution. In conclusion, CO_2-assisted pyrolysis is a promising method to produce the Fe-biochar composite adsorbent derived from waste materials for recovery of fuel gases and for fabrication of adsorbent materials with enhanced functionality to simultaneously treat cationic and anionic heavy metals.

Acknowledgment

References

Affandi, F. A., Ishak, M. Y., 2019. Impacts of suspended sediment and metal pollution from mining activities on riverine fish population—a review. Environ. Sci. Pollut. Res. 26**,** 16939-16951.

Akcil, A., Erust, C., Ozdemiroglu, S., Fonti, V., Beolchini, F., 2015. A review of approaches and techniques used in aquatic contaminated sediments: metal removal and stabilization by chemical and biotechnological processes. J. Clean Prod. 86**,** 24-36.

Al-Kaabi, M. A., Al-Ghouti, M. A., Ashfaq, M. Y. M., Ahmed, T., Zouari, N., 2019. An integrated

approach for produced water treatment using microemulsions modified activated carbon. J. Water Process. Eng. 31, 100830.

Beck, R., Bommarito, P., Douillet, C., Kanke, M., Del Razo, L. M., García-Vargas, G., Fry, R. C., Sethupathy, P., Stýblo, M., 2018. Circulating miRNAs Associated with Arsenic Exposure. Environ. Sci. Technol. 52, 14487-14495.

Bian, L., Nie, J., Jiang, X., Song, M., Dong, F., Shang, L., Deng, H., He, H., Belzile, N., Chen, Y., Xu, B., Liu, X., 2019. Selective adsorption of uranyl and potentially toxic metal ions at the core-shell MFe_2O_4-TiO_2 (M=Mn, Fe, Zn, Co, or Ni) nanoparticles. J. Hazard. Mater. 365, 835-845.

Cho, D.-W., Jeon, B.-H., Jeong, Y., Nam, I.-H., Choi, U.-K., Kumar, R., Song, H., 2016. Synthesis of hydrous zirconium oxide-impregnated chitosan beads and their application for removal of fluoride and lead. Appl. Surf. Sci. 372, 13-19.

Cho, D.-W., Yoon, K., Ahn, Y., Sun, Y., Tsang, D. C. W., Hou, D., Ok, Y. S., Song, H., 2019. Fabrication and environmental applications of multifunctional mixed metal-biochar composites (MMBC) from red mud and lignin wastes. J. Hazard. Mater. 374, 412-419.

Dawood, S., Sen, T. K., Phan, C., 2017. Synthesis and characterization of slow pyrolysis pine cone bio-char in the removal of organic and inorganic pollutants from aqueous solution by adsorption: Kinetic, equilibrium, mechanism and thermodynamic. Bioresour. Technol. 246, 76-81.

Daza, Y. A., Kent, R. A., Yung, M. M., Kuhn, J. N., 2014. Carbon Dioxide Conversion by Reverse Water–Gas Shift Chemical Looping on Perovskite-Type Oxides. Ind. Eng. Chem. Res. 53, 5828-5837.

Deng, M., Kuo, D. T. F., Wu, Q., Zhang, Y., Liu, X., Liu, S., Hu, X., Mai, B., Liu, Z., Zhang, H., 2018. Organophosphorus flame retardants and heavy metals in municipal landfill leachate treatment system in Guangzhou, China. Environ. Pollut. 236, 137-145.

Deng, Y., Huang, S., Laird, D. A., Wang, X., Meng, Z., 2019. Adsorption behaviour and mechanisms of cadmium and nickel on rice straw biochars in single- and binary-metal systems. Chemosphere. 218, 308-318.

Di, Z., Cao, Y., Yang, F., Zhang, K., Cheng, F., 2019. Thermodynamic analysis on the parametric optimization of a novel chemical looping methane reforming in the separated productions of H_2 and CO. Energy Conv. Manag. 192**,** 171-179.

do Prado, N. T., Heitmann, A. P., Mansur, H. S., Mansur, A. A., Oliveira, L. C. A., de Castro, C. S., 2017. PET-modified red mud as catalysts for oxidative desulfurization reactions. J. Environ. Sci. 57**,** 312-320.

Erol, S., Özdemir, M., 2016. Removal of nickel from aqueous solution using magnesite tailing. Desalin. Water Treat. 57**,** 5810-5820.

Feng, Y., Wu, D., Liao, C., Deng, Y., Zhang, T., Shih, K., 2016. Red mud powders as low-cost and efficient catalysts for persulfate activation: Pathways and reusability of mineralizing sulfadiazine. Sep. Purif. Technol. 167**,** 136-145.

Gong, J., Lee, C.-S., Kim, E.-J., Chang, Y.-Y., Chang, Y.-S., 2016. Enhancing the reactivity of bimetallic Bi/Fe^0 by citric acid for remediation of polluted water. J. Hazard. Mater. 310**,** 135-142.

Huang, Y., Zhang, W., Zhang, M., Zhang, X., Zhao, Y., 2018. Hydroxyl-functionalized $TiO_2@SiO_2@Ni/nZVI$ nanocomposites fabrication, characterization and enhanced simultaneous visible light photocatalytic oxidation and adsorption of arsenite. Chem. Eng. J. 338**,** 369-382.

Ihsanullah, Abbas, A., Al-Amer, A. M., Laoui, T., Al-Marri, M. J., Nasser, M. S., Khraisheh, M., Atieh, M. A., 2016. Heavy metal removal from aqueous solution by advanced carbon nanotubes: Critical review of adsorption applications. Sep. Purif. Technol. 157**,** 141-161.

Inchaurrondo, N., di Luca, C., Mori, F., Pintar, A., Žerjav, G., Valiente, M., Palet, C., 2019. Synthesis and adsorption behavior of mesoporous alumina and Fe-doped alumina for the removal of dominant arsenic species in contaminated waters. J. Environ. Chem. Eng. 7**,** 102901.

Jacob, J. M., Karthik, C., Saratale, R. G., Kumar, S. S., Prabakar, D., Kadirvelu, K., Pugazhendhi, A., 2018. Biological approaches to tackle heavy metal pollution: A survey of literature. J. Environ. Manage. 217**,** 56-70.

Jemutai-Kimosop, S., Orata, F., Shikuku, V. O., Okello, V. A., Getenga, Z. M., 2020. Insights on adsorption of carbamazepine onto iron oxide modified diatomaceous earth: Kinetics, isotherms, thermodynamics, and mechanisms. Environ. Res. 180**,** 108898.

Jeon, E.-K., Ryu, S., Park, S.-W., Wang, L., Tsang, D. C. W., Baek, K., 2018. Enhanced adsorption of arsenic onto alum sludge modified by calcination. J. Clean Prod. 176**,** 54-62.

Jiang, D., Yang, Y., Huang, C., Huang, M., Chen, J., Rao, T., Ran, X., 2019. Removal of the heavy metal ion nickel (II) via an adsorption method using flower globular magnesium hydroxide. J. Hazard. Mater. 373**,** 131-140.

Khan, U. A., Kujala, K., Nieminen, S. P., Räisänen, M. L., Ronkanen, A.-K., 2019. Arsenic, antimony, and nickel leaching from northern peatlands treating mining influenced water in cold climate. Sci. Total Environ. 657**,** 1161-1172.

Kheirandish, S., Ghaedi, M., Dashtian, K., Jannesar, R., Montazerozohori, M., Pourebrahim, F., Zare, M. A., 2017. Simultaneous removal of Cd(II), Ni(II), Pb(II) and Cu(II) ions via their complexation with HBANSA based on a combined ultrasound-assisted and cloud point adsorption method using CSG-BiPO4/FePO$_4$ as novel adsorbent: FAAS detection and optimization process. J. Colloid Interface Sci. 500**,** 241-252.

Kołodyńska, D., Krukowska, J., Thomas, P., 2017. Comparison of sorption and desorption studies of heavy metal ions from biochar and commercial active carbon. Chem. Eng. J. 307**,** 353-363.

Kumar, A. S. K., Jiang, S.-J., 2016. Chitosan-functionalized graphene oxide: A novel adsorbent an efficient adsorption of arsenic from aqueous solution. J. Environ. Chem. Eng. 4**,** 1698-1713.

Kumar, S., Prasad, S., Yadav, K. K., Shrivastava, M., Gupta, N., Nagar, S., Bach, Q.-V., Kamyab, H., Khan, S. A., Yadav, S., Malav, L. C., 2019. Hazardous heavy metals contamination of vegetables and food chain: Role of sustainable remediation approaches - A review. Environ. Res. 179**,** 108792.

Lee, J., Choi, D., Tsang, Y. F., Oh, J.-I., Kwon, E. E., 2017. Employing CO$_2$ as reaction medium for in-situ suppression of the formation of benzene derivatives and polycyclic aromatic hydrocarbons

during pyrolysis of simulated municipal solid waste. Environ. Pollut. 224**,** 476-483.

Li, H., Dong, X., da Silva, E. B., de Oliveira, L. M., Chen, Y., Ma, L. Q., 2017a. Mechanisms of metal sorption by biochars: Biochar characteristics and modifications. Chemosphere. 178**,** 466-478.

Li, J., Wang, X., Zhao, G., Chen, C., Chai, Z., Alsaedi, A., Hayat, T., Wang, X., 2018. Metal–organic framework-based materials: superior adsorbents for the capture of toxic and radioactive metal ions. Chem. Soc. Rev. 47**,** 2322-2356.

Li, P., Li, D., Yang, H., Wang, X., Chen, H., 2016. Effects of Fe-, Zr-, and Co-Modified Zeolites and Pretreatments on Catalytic Upgrading of Biomass Fast Pyrolysis Vapors. Energy Fuels. 30**,** 3004-3013.

Li, S.-S., Jiang, M., Jiang, T.-J., Liu, J.-H., Guo, Z., Huang, X.-J., 2017b. Competitive adsorption behavior toward metal ions on nano-Fe/Mg/Ni ternary layered double hydroxide proved by XPS: Evidence of selective and sensitive detection of Pb(II). J. Hazard. Mater. 338**,** 1-10.

Li, S., Wang, W., Liang, F., Zhang, W.-x., 2017c. Heavy metal removal using nanoscale zero-valent iron (nZVI): Theory and application. J. Hazard. Mater. 322**,** 163-171.

Liu, L., Zhang, Y., He, Y., Xie, Y., Huang, L., Tan, S., Cai, X., 2015a. Preparation of montmorillonite-pillared graphene oxide with increased single- and co-adsorption towards lead ions and methylene blue. RSC Adv. 5**,** 3965-3973.

Liu, S., Kang, S., Wang, G., Zhao, H., Cai, W., 2015b. Micro/nanostructured porous Fe–Ni binary oxide and its enhanced arsenic adsorption performances. J. Colloid Interface Sci. 458**,** 94-102.

Liu, X., Sun, J., Duan, S., Wang, Y., Hayat, T., Alsaedi, A., Wang, C., Li, J., 2017. A Valuable Biochar from Poplar Catkins with High Adsorption Capacity for Both Organic Pollutants and Inorganic Heavy Metal Ions. Sci Rep. 7**,** 10033.

Long, X., Chen, R., Tan, J., Lu, Y., Wang, J., Huang, T., Lei, Q., 2020. Electrochemical recovery of cobalt using nanoparticles film of copper hexacyanoferrates from aqueous solution. J. Hazard. Mater. 384**,** 121252.

Lu, W., Li, J., Sheng, Y., Zhang, X., You, J., Chen, L., 2017. One-pot synthesis of magnetic iron oxide nanoparticle-multiwalled carbon nanotube composites for enhanced removal of Cr(VI) from aqueous solution. J. Colloid Interface Sci. 505**,** 1134-1146.

Mahdi, Z., Yu, Q. J., El Hanandeh, A., 2018. Investigation of the kinetics and mechanisms of nickel and copper ions adsorption from aqueous solutions by date seed derived biochar. J. Environ. Chem. Eng. 6**,** 1171-1181.

Nasir, A. M., Goh, P. S., Ismail, A. F., 2018. Novel synergistic hydrous iron-nickel-manganese (HINM) trimetal oxide for hazardous arsenite removal. Chemosphere. 200**,** 504-512.

Nath, H., Sahoo, P., Sahoo, A., 2015. Characterization of Red Mud treated under high temperature fluidization. Powder Technol. 269**,** 233-239.

Öman, C. B., Junestedt, C., 2008. Chemical characterization of landfill leachates – 400 parameters and compounds. Waste Manage. 28**,** 1876-1891.

Ray, P. Z., Shipley, H. J., 2015. Inorganic nano-adsorbents for the removal of heavy metals and arsenic: a review. RSC Adv. 5**,** 29885-29907.

Shakya, A. K., Paul, S., Ghosh, P. K., 2019. Bio-attenuation of arsenic and iron coupled with nitrate remediation in multi-oxyanionic system: Batch and column studies. J. Hazard. Mater. 375**,** 182-190.

Shen, C., Zhao, Y., Li, W., Yang, Y., Liu, R., Morgen, D., 2019. Global profile of heavy metals and semimetals adsorption using drinking water treatment residual. Chem. Eng. J. 372**,** 1019-1027.

Shen, Y., Ma, D., Ge, X., 2017. CO2-looping in biomass pyrolysis or gasification. Sustain. Energ. Fuels. 1**,** 1700-1729.

Sigdel, A., Park, J., Kwak, H., Park, P.-K., 2016. Arsenic removal from aqueous solutions by adsorption onto hydrous iron oxide-impregnated alginate beads. J. Ind. Eng. Chem. 35**,** 277-286.

Siles, J. A., Vargas, F., Gutiérrez, M. C., Chica, A. F., Martín, M. A., 2016. Integral valorisation of waste orange peel using combustion, biomethanisation and co-composting technologies. Bioresour.

Technol. 211**,** 173-182.

Sizmur, T., Fresno, T., Akgül, G., Frost, H., Moreno-Jiménez, E., 2017. Biochar modification to enhance sorption of inorganics from water. Bioresour. Technol. 246**,** 34-47.

Soni, R., Shukla, D. P., 2019. Synthesis of fly ash based zeolite-reduced graphene oxide composite and its evaluation as an adsorbent for arsenic removal. Chemosphere. 219**,** 504-509.

Sun, Y., Yu, I. K. M., Tsang, D. C. W., Cao, X., Lin, D., Wang, L., Graham, N. J. D., Alessi, D. S., Komárek, M., Ok, Y. S., Feng, Y., Li, X.-D., 2019. Multifunctional iron-biochar composites for the removal of potentially toxic elements, inherent cations, and hetero-chloride from hydraulic fracturing wastewater. Environ. Int. 124**,** 521-532.

Tanboonchuy, V., Hsu, J.-C., Grisdanurak, N., Liao, C.-H., 2011. Gas-bubbled nano zero-valent iron process for high concentration arsenate removal. J. Hazard. Mater. 186**,** 2123-2128.

Tripathi, M., Sahu, J. N., Ganesan, P., 2016. Effect of process parameters on production of biochar from biomass waste through pyrolysis: A review. Renew. Sust. Energ. Rev. 55**,** 467-481.

Wang, S., Gao, B., Li, Y., 2016. Enhanced arsenic removal by biochar modified with nickel (Ni) and manganese (Mn) oxyhydroxides. J. Ind. Eng. Chem. 37**,** 361-365.

Wu, G., Ma, J., Li, S., Guan, J., Jiang, B., Wang, L., Li, J., Wang, X., Chen, L., 2018. Magnetic copper-based metal organic framework as an effective and recyclable adsorbent for removal of two fluoroquinolone antibiotics from aqueous solutions. J. Colloid Interface Sci. 528**,** 360-371.

Xu, J., Cao, Z., Zhang, Y., Yuan, Z., Lou, Z., Xu, X., Wang, X., 2018. A review of functionalized carbon nanotubes and graphene for heavy metal adsorption from water: Preparation, application, and mechanism. Chemosphere. 195**,** 351-364.

Xu, X., Chen, W., Zong, S., Ren, X., Liu, D., 2019. Atrazine degradation using Fe_3O_4-sepiolite catalyzed persulfate: Reactivity, mechanism and stability. J. Hazard. Mater. 377**,** 62-69.

Yang, Q., Wang, J., Zhang, W., Liu, F., Yue, X., Liu, Y., Yang, M., Li, Z., Wang, J., 2017. Interface engineering of metal organic framework on graphene oxide with enhanced adsorption capacity for

organophosphorus pesticide. Chem. Eng. J. 313**,** 19-26.

Yoon, K., Lee, S. S., Ok, Y. S., Kwon, E. E., Song, H., 2019. Enhancement of syngas for H_2 production via catalytic pyrolysis of orange peel using CO_2 and bauxite residue. Appl. Energy. 254**,** 113803.

Highlights

- Co-pyrolysis of red mud and orange peel in N_2 and CO_2 environments

- Adsorption comparison of pollutants [As(V) and Ni(II)] by two Fe-biochars

- Different adsorption behaviors of As(V) and Ni(II) in single- and binary systems

- Enhanced adsorption ability of Fe-biochar by the coexistence of As(V) and Ni(II)

CRediT authorship contribution statement

Kwangsuk Yoon: Conceptualization, Data curation, Writing-original draft, **Dong-Wan Cho**: Methodology, Data curation, Visualization, Writing-review. **Amit Bhatnagar**: Validation, Methodology. **Hocheol Song**: Writing-review & editing, Supervision

Declaration of interests

☒ The authors declare that they have no known competing financial interests or personal relationships that could have appeared to influence the work reported in this paper.

☐The authors declare the following financial interests/personal relationships which may be considered as potential competing interests: